Quentin Douasbin, Matthias Ihme, Christoph Arndt

Pareto-efficient combustion framework for predicting transient ignition dynamics in turbulent flames: Application to a pulsed jet-in-hot-coflow flame

Combustion and Flame 223 (2021), 153-165.

The original publication is available at www.elsevier.com

https://doi.org/10.1016/j.combustflame.2020.09.031

Pareto-efficient combustion framework for predicting transient ignition dynamics in turbulent flames: Application to a pulsed jet-in-hot-coflow flame

Quentin Douasbin[a,*], Matthias Ihme[a,b], Christoph Arndt[c]

[a] *Center for Turbulence Research, Stanford University, Stanford, CA 94305, United States*
[b] *Department of Mechanical Engineering, Stanford University, Stanford, CA 94305, United States*
[c] *German Aerospace Center (DLR), Institute of Combustion Technology, Stuttgart, Germany*

Abstract

The Pareto-efficient combustion (PEC) framework is extended for predicting transient ignition in turbulent flames. The PEC formulation utilizes a drift term to assess the compliance of specific combustion submodels with the underlying flow-field representation. This drift term is extended to consider autoignition delay as a process of interest, and the ignition delay time of a homogeneous isobaric reactor is utilized as surrogate. Combustion models considered are the steady-state flamelet/progress variable (FPV) model and a finite-rate chemistry (FRC) model. Large-eddy simulations are performed and the proposed PEC autoignition formulation (PEC-AI) is demonstrated to identify localized regions that require a finite-rate chemistry description in order to accurately capture the transient ignition dynamics. The model is employed to examine the stochasticity of the autoignition in the turbulent environment by performing ensemble simulations to construct probability distributions of ignition time and ignition locations. Comparisons with measurements show the ability of PEC-AI in capturing the transient ignition dynamics and flame lift-off through drift-term adaptation with comparable accuracy to FRC simulations at reduced cost. These results illustrate the versatility of the PEC framework in targeting different combustion response functions that not only include species and emissions but also transient combustion processes.

Keywords: Pareto-efficient combustion framework, Large-eddy simulation, Autoignition, Turbulent combustion, Jet-in-hot-coflow

1. Introduction

Autoignition (AI) plays a critical role in flame stabilization, such as diesel fuel ignition, vitiated flows, industrial furnaces, or staged combustors [1, 2]. In the presence of turbulence and unsteady mixing, autoignition is a stochastic process that requires the consideration of the local mixture composition and temperature, the turbulent flow environment, and detailed reaction chemistry.

Flame stabilization by autoignition in lifted flames has been studied experimentally and computationally in jet-in-hot-coflow (JHC) configurations with well-defined boundary conditions [3, 4, 5, 6]. Lifted flames are highly sensitive to the composition and temperature of the vitiated coflow [2]

*Corresponding author:
Email addresses: douasbin@stanford.edu (Quentin Douasbin), mihme@stanford.edu (Matthias Ihme)

and accurately capturing the lift-off height over a wide range of operating conditions is challenging for combustion models. In particular, a relatively low coflow temperature tends to increase the flame lift-off height, and these conditions are most difficult to predict. In these investigations, it was found that the lift-off height increases with jet and coflow velocities and decreases with increasing coflow temperature [3, 7]. To model autoignition in a vitiated flame, Domingo et al. [4] developed a tabulated chemistry model that combines a homogeneous reactor (HR) ignition model for representing the autoignition regime with a premixed flamelet formulation for capturing the downstream flame structure. This approach was shown to improve the prediction of the flame base that is controlled by autoignition, while downstream regions that are represented by non-premixed regimes show discrepancies with measurements. An unsteady flamelet/progress-variable model was developed in [5]. In this model, the scalar dissipation rate was introduced and the thermochemical flame state was then calculated from the solution of unsteady flamelet equations to describe the transient ignition dynamics. Compared to results obtained from a steady-state flamelet model, this approach led to accurate predictions of the flame lift-off height and species profiles. Both models [4, 5] employed presumed probability density functions (PDFs) as closure models for representing the turbulence-chemistry interaction. More recently, Schulz et al. [6] used a reduced chemistry model and a dynamically thickened flame model to describe autoignition in a lifted flame. Statistical results compared favorably with measurements but an overprediction of the lift-off height was reported.

Transient autoignition was studied experimentally using a pulsed methane JHC configuration [2, 7, 8, 9, 10, 11, 12, 13]. Different fuels (methane, propane, dimethyl ether) were used and several operating conditions with various coflow temperatures were investigated. Stochastic features of the autoignition dynamics were reported by Arndt et al. [12] in the form of PDFs of autoignition time and ignition location. This configuration was numerically examined using different modeling approaches [14, 15, 16]. Fiolitakis and Arndt [14] employed a transported PDF model and a k-ϵ turbulence model to simulate the statistically stationary flame behavior. While the mean flame structure agrees relatively well with experiments, discrepancies were found for the Root Mean Square (RMS) profiles. Inanc and Kempf [15] used a steady flamelet-based combustion models to study the transient and stochastic features of autoignition. These simulations reproduced the locations of the transient ignition kernels and ignition time with good accuracy, but the flame lift-off height was under-predicted in these simulations. Liu et al. [16] used a finite rate chemistry model along with a partially stirred reactor model to account for turbulence-chemistry interactions. Although the jet penetration length and the jet spreading angle are mispredicted, their results agree well with the experiments and it was found that the regions of highest heat release rate and temperature are located in the flame propagation region. An analysis of the transient ignition kernels was performed and it was shown that the Damköhler number is larger in the auto-ignition region than in the flame-propagation regions that develops further downstream.

The prediction of autoignition and flame stabilization in non-premixed turbulent flames requires the consideration of multi-mode combustion regimes [4, 5]. Autoignition in vitiated flames is initiated in regions of low scalar dissipation rate with species composition corresponding to the most reactive mixture [17]. Subsequently, heat and radicals diffuse towards richer mixtures that combust in an opposed mixing mode [18] followed by a diffusion-dominated combustion regime [6]. Lean and rich propagating flames are present near the centerline [4]. Hence, in order to accurately model these flames, adaptive combustion models are needed that describe the transient ignition dynamics and multi-mode combustion behavior.

An adaptive combustion modeling approach in the form of the Pareto-efficient combustion (PEC) framework was recently developed to model multi-mode combustion [19, 20, 21]. This framework employs a combustion submodel assignment to describe different combustion regimes. In this formulation, the compliance of combustion models to the underlying flow physics is assessed through the construction of a so-called drift term, which takes into consideration user-specific requirements about Quantities of Interest (QoI) and computational cost. So far, this formulation is limited to scalar flow-field quantities, such as species mass fractions, and model extensions are needed to accurately describe autoignition and transient combustion processes. By addressing this need, the objective of this work is to extend the PEC formulation to the prediction of autoignition in turbulent unsteady flames. To this end, we consider the autoignition delay time as a physical Process of Interest (PoI) and the drift-term formulation is extended to consider this process as a controlling parameter. This formulation is applied to the DLR-JHC configuration [12].

The remainder of this manuscript has the following structure. Section 2 presents the PEC framework, and its extension to autoignition is discussed in Sec. 3. The experimental configuration and numerical setup are presented in Sec. 4. In Sec. 5, PEC is applied to the DLR-JHC configuration and the model mapping is analyzed and compared to monolithic FPV and FRC calculations, before analyzing both statistically stationary flame and stochastic ignition characteristics via ensemble calculations. The manuscript closes with conclusions.

2. Governing equations and PEC-formulation

In this study, the fully compressible Navier-Stokes equations for reacting flows are solved. The system of Favre-filtered conservation equations for mass, momentum and energy for LES take the following form:

$$\widetilde{D}_t\bar{\rho} = -\bar{\rho}\nabla\cdot\widetilde{\boldsymbol{u}}\,, \tag{1a}$$

$$\bar{\rho}\widetilde{D}_t\widetilde{\boldsymbol{u}} = -\nabla\bar{p}+\nabla\cdot\left(\overline{\boldsymbol{\tau}}+\boldsymbol{\tau}_{\mathrm{sgs}}\right)\,, \tag{1b}$$

$$\bar{\rho}\widetilde{D}_t\widetilde{e} = -\nabla\cdot\left(\widetilde{\boldsymbol{u}}\bar{p}\right)+\nabla\cdot\left(\overline{\boldsymbol{\tau}}\cdot\widetilde{\boldsymbol{u}}\right)-\nabla\cdot\left(\overline{\boldsymbol{q}}+\boldsymbol{q}_{\mathrm{sgs}}\right)\,, \tag{1c}$$

where $\widetilde{D}_t = \partial/\partial t + \widetilde{\boldsymbol{u}}\cdot\nabla$ is the material derivative, ρ is the density, $\boldsymbol{u}$ is the velocity vector, p is the pressure, e is the specific total energy, $\boldsymbol{\tau}$ is the stress tensor, $\boldsymbol{q}$ is the heat flux, and the subscript 'sgs' refers to a turbulent subgrid scale quantity. The LES scalar transport equations take the following form:

$$\bar{\rho}\widetilde{D}_t\widetilde{\boldsymbol{\phi}} = -\nabla\cdot\left(\overline{\boldsymbol{j}}+\boldsymbol{j}_{\mathrm{sgs}}\right)+\overline{\dot{\boldsymbol{S}}}_\phi\,, \tag{2}$$

where $\widetilde{\boldsymbol{\phi}} = \left[\widetilde{\phi}^{m_1},\ldots,\widetilde{\phi}^{m_N}\right]^{\mathsf{T}}$ combines the scalar solution vectors of the m_N submodels considered by PEC, $M=\{m_1,\ldots,m_N\}$, and $\overline{\dot{\boldsymbol{S}}}_\phi$ is the vector of filtered chemical source terms.

In the present study, two submodels are considered. The first model is the Flamelet/Progress Variable (FPV) formulation [22, 23], where the mixture fraction Z and a progress variable C are transported, $\widetilde{\boldsymbol{\phi}}^{m_1} = \widetilde{\boldsymbol{\phi}}^{\mathrm{FPV}} = \left[\widetilde{Z},\widetilde{C}\right]^{\mathsf{T}}$. The second model is a Finite Rate Chemistry (FRC) model for which N_s-1 species mass fractions are transported and the $N_s{}^{\mathrm{th}}$ species mass fraction is inferred from total mass conservation:

$$\widetilde{Y}_{N_s} = 1-\sum_{k=1}^{N_s-1}\widetilde{Y}_k\,, \tag{3}$$

and the vector of transport species is $\widetilde{\boldsymbol{\phi}}^{m_2} = \widetilde{\boldsymbol{\phi}}^{\mathrm{FRC}} = [\widetilde{Y}_1, \ldots, \widetilde{Y}_{N_s-1}]^\intercal$.

PEC employs a submodels assignment $\mathcal{M}$ that maps the computational domain Ω to the set of models M, here, $M = \{m_1, m_2\}$. The domain is partitioned into N_p subdomains $\bar{\Omega}_i$ with a boundary $\partial\Omega_i$ and an interior Ω_i, such that $\bar{\Omega}_i = \Omega_i \cup \partial\Omega_i$. This submodel mapping uniquely determines the partitions and satisfies the following properties:

1. The entire domain is recovered by the subdomains: $\cup_{i=1}^{N_p} \bar{\Omega}_i = \bar{\Omega}$,
2. The subdomains are non-overlapping: $\Omega_i \cap \Omega_j = \emptyset \quad \forall i \neq j$,
3. In each subdomain, a single model is used: $\mathcal{M}(\boldsymbol{x}) = \mathcal{M}(\boldsymbol{y}) \quad \forall \boldsymbol{x} \in \Omega_i, \boldsymbol{y} \in \Omega_i$,
4. All subdomains that are separated by a common boundary use different models, $\mathcal{M}(\boldsymbol{x}) \neq \mathcal{M}(\boldsymbol{y}) \quad \forall i \neq j, \boldsymbol{x} \in \Omega_i, \boldsymbol{y} \in \Omega_j, \partial\Omega_i \cap \partial\Omega_j \neq \emptyset$.

The thermochemical state is evaluated from the manifold-describing variables as well as the reconstruction of the scalar transport equation for model coupling [19], which is further discussed in Wu et al. [21].

The PEC framework utilizes a local optimization to obtain a submodel assignment $\mathcal{M}$, at a given time t:

$$\min_{\mathcal{M}:\Omega\to M} \underbrace{\int_\Omega e^{\mathcal{M}}(\boldsymbol{x}) d\boldsymbol{x}}_{\text{global error } \mathcal{E}} + \lambda \underbrace{\int_\Omega c^{\mathcal{M}}(\boldsymbol{x}) d\boldsymbol{x}}_{\text{global cost } \mathcal{C}} \tag{4}$$

where $e^{\mathcal{M}}(\boldsymbol{x})$ and $c^{\mathcal{M}}(\boldsymbol{x})$ are the local error and cost of the model mapping and the user-defined parameter λ is a penalty term that balances cost and accuracy. In practice, Eq. (4) is solved via a greedy strategy [19]. In previous studies [19, 20, 21], a set of user-specific QoIs, $Q = \{\widetilde{\psi}_1, \ldots, \widetilde{\psi}_{N_Q}\}$, is defined and the local error $e^{\mathcal{M}}$ is evaluated from the weighted sum of errors of each QoI $\widetilde{\psi} \in Q$:

$$e^{\mathcal{M}} = \sum_{\psi \in Q} \xi_\psi \left| \widetilde{\mathcal{D}}_\psi^{\mathcal{M}} \right| , \tag{5}$$

where $\widetilde{\mathcal{D}}_\psi^{\mathcal{M}}$ is the drift term of QoI $\widetilde{\psi}$ and $\xi_\psi > 0$ is a normalization constant [19] so that the error associated with each QoI is of order of unity.

The drift term provides a formal method for assessing the compliance of a combustion model with the underlying flow-field description via the evaluation of the growth rate of the error of a candidate submodel. The drift term associated with submodel $m = \mathcal{M}(\boldsymbol{x})$ for a QoI $\widetilde{\psi}$ is [19]:

$$\widetilde{\mathcal{D}}_\psi^m = \bar{\rho} \widetilde{D}_t \widetilde{\psi} \Big|_{\widetilde{\psi} = \widetilde{\psi}^m} - \bar{\rho} \widetilde{D}_t \widetilde{\psi}^m , \tag{6}$$

where $\widetilde{\psi}^m$ is the QoI evaluated on the manifold solution of model m. On the right-hand side of Eq. (6), the first term is the material derivative of QoI $\widetilde{\psi}$, evaluated from the solution of the transport equation with initial conditions $\widetilde{\psi} = \widetilde{\psi}^m$, *i.e.* the current state of the flow field. The second term is the material derivative of $\widetilde{\psi}^m$ predicted from the manifold-describing variables $\widetilde{\boldsymbol{\phi}}^m$. By employing the chain rule, this term can be computed as:

$$\bar{\rho} \widetilde{D}_t \widetilde{\psi}^m = \bar{\rho} \frac{\partial \widetilde{\psi}^m}{\partial \widetilde{\boldsymbol{\phi}}^m} \cdot \widetilde{D}_t \widetilde{\boldsymbol{\phi}}^m \qquad \text{where} \quad \widetilde{\psi}^m = \widetilde{\psi}^m \left(\widetilde{\boldsymbol{\phi}}^m \right) . \tag{7}$$

The difference between these quantities provides a direct measure of the compliance between a particular combustion model and the underlying flow field description. In this context, it is noted that

the PEC formulation only assesses the compliance of a combustion manifold with the underlying flow field representation and employs a hierarchical submodel formulation. Here, we consider FRC as the model of highest fidelity, as discussed in Sec. 4.2.2. Although only two combustion models are considered in the present work, the PEC framework can be applied to an arbitrary number of models, which has been demonstrated in prior studies [19].

3. PEC extension to a process of interest

Autoignition in turbulent flames is a dynamic and non-local combustion process. As such, the previous QoI-based PEC formulation cannot be directly used for this purpose. By addressing this issue, the objective of this section is to extend the PEC formulation to consider a Process of Interest (PoI) and derive a drift term that takes into consideration transient combustion processes.

3.1. Drift term for a process of interest

In many practical applications, the design parameters involve non-trivial physical processes, such as heat flux, heat release, or autoignition time. These secondary quantities cannot be directly obtained as a solution of a transport equation. To represent these secondary quantities in the PEC formulation, we introduce a process of interest, π, and consider its scalar dependencies, *i.e.*, $\pi = \pi(\psi_{\pi,1}, \ldots, \psi_{\pi,N_\pi})$, to construct a drift term. By employing the chain rule, the resulting drift term, evaluated for the m^{th} submodel, can then be written as:

$$\widetilde{\mathcal{D}}_\pi^m = \sum_{i=1}^{N_\pi} \widetilde{\frac{\partial \pi}{\partial \psi_{\pi,i}} \mathcal{D}_{\psi_{\pi,i}}^m} \ , \tag{8}$$

where $\partial\pi/\partial\psi_{\pi,i}$ is the sensitivity coefficient of π. A detailed analysis of the extension of the laminar drift term to LES can be found in [20]. With this, the local error for π can be evaluated by normalizing $\widetilde{\mathcal{D}}_\pi^m$ as:

$$e^m = \xi_\pi \left| \widetilde{\mathcal{D}}_\pi^m \right| \ , \tag{9}$$

where the normalization coefficient $\xi_\pi > 0$ is determined from pre-processed quantities. In the present work, we defined ξ_π as

$$\xi_\pi = \left[\sum_{i=1}^{N_\pi} \left(\max\left(\frac{\partial \pi}{\partial \psi_{\pi,i}} \right) \ \max\left(\dot{S}_{\psi_{\pi,i}} \right) \right) \right]^{-1} \ , \tag{10}$$

which considers the directional sensitivity coefficient and the production rate of species $\psi_{\pi,i}$. This normalization ensures that the maximum of the drift term for a PoI is of order unity. It is noted that the maxima of both terms in Eq. (10) may correspond to different thermochemical states. Here, the normalization coefficients are obtained from the FPV-model and are precomputed from the flamelet library.

3.2. Autoignition time of a turbulent jet-in-hot-coflow flame

The focus of this study is to predict the autoignition in a JHC-burner. As discussed by Mastorakos [24] and observed experimentally [3, 10, 11, 12], in vitiated non-premixed flames, autoignition occurs away from the stoichiometric mixture at very lean conditions, corresponding to the so-called most reactive mixture fraction Z_{mr}. However, not all regions with $Z = Z_{\text{mr}}$ ignite and

autoignition sites are found in regions with low scalar dissipation rate, χ [24]. Hence, in turbulent non-premixed flames, autoignition sites are distributed according to the local scalar dissipation rate. In addition, it was found that the autoignition time, τ_{AI}, is larger than the autoignition delay time of a homogeneous reactor, τ_{ig}, that is $\tau_{\mathrm{AI}} > \tau_{\mathrm{ig}}$. Consistent with this analysis, Arndt et al. [12] reported that in a JHC configuration the fuel is transported into the vitiation coflow where it mixes with the oxidizer in intermittent regions of low turbulence, forming an ignitable mixture.

With this understanding about the autoignition process, the PEC framework is extended to capture the autoignition. For this, we consider the autoignition time, τ_{AI}, as a process of interest. Since the direct derivation and solution of a transport equation for τ_{AI} is non-trivial, we consider a surrogate that closely represents the physical PoI, $\pi_{\mathrm{phys}} \simeq \pi_{\mathrm{surr}}$. Therefore, we represent τ_{AI} by the ignition delay of a homogeneous isobar reactor, with mixture composition prescribed from a non-premixed flamelet solution, $\tau_{\mathrm{AI}} \simeq \tau_{\mathrm{ig}}$, with $\tau_{\mathrm{ig}}(\boldsymbol{\psi}_\pi)$. For diffusion flames, it was shown that the autoignition time is a function of temperature, composition and scalar dissipation rate [24]. However, Eq. (8) indicates that the contribution of any quantity to the drift term of a PoI is the product of two terms. As shown in [5], τ_{ig} only exhibits a weak dependency on the scalar dissipation so that the first term, the sensitivity coefficient, is small. The second term is the drift term of the scalar dissipation rate itself, which would require an additional of a transport equation. Since the scalar dissipation rate would be computed irrespectively from the submodel m, the drift term would be $\widetilde{\mathcal{D}}_\chi^m = 0$.

In the FPV model, which is employed as one of the submodels, the thermochemical state is parameterized in terms of mixture fraction Z and progress variable C, which is evaluated as $C = Y_{\mathrm{CO_2}} + Y_{\mathrm{CO}} + Y_{\mathrm{H_2O}} + Y_{\mathrm{H_2}}$ [25]. However, this model employs a steady-state flamelet formulation which is unable to predict autoignition [23]. Here, we show how to extend the analysis in order to identify the leading sensitivities of τ_{ig}. For this, a sensitivity analysis of τ_{ig} at the most reactive mixture fraction Z_{mr} is performed. First, Z_{mr} is identified by conducting Cantera simulations of isobaric HR along the mixing line, leading to a value of $Z_{\mathrm{mr}} = 0.0048$. This value was confirmed by performing an additional unsteady flamelet simulation of a counterflow diffusion flame at low scalar dissipation rate. Then, the thermochemical state corresponding to the most reactive mixture fraction was perturbed, by adding 1% of the maximum mass fraction of a species Y_k during a HR simulation at the most reacting conditions, to compute the sensitivity coefficients $\partial\tau_{\mathrm{ig}}/\partial Y_k$. Results from this sensitivity analysis showed that the largest sensitivity of τ_{ig} arises from variations in Y_{OH}. Based on this analysis, hydroxyl is included as an additional independent variable of the autoignition delay time. In addition, the autoignition time was shown to be sensitive to the temperature, so that this quantity is added as an additional independent variable. From this analysis, it follows that $\pi = \tau_{\mathrm{ig}}(\boldsymbol{\psi}_\pi)$ with $\boldsymbol{\psi}_\pi = \{Z, C, T, Y_{\mathrm{OH}}\}$. The sensitivity coefficients in Eq. (8) are then computed using the composition from the flamelet solutions and perturbations of this manifold with respect to T and Y_{OH}.

Figure 1 shows results that are utilized for the evaluation of the sensitivity coefficients, and the computed sensitivity coefficient are illustrated in Fig. 2. In the first step, the sensitivity coefficients for $\partial\tau_{\mathrm{ig}}/\partial Z$ and $\partial\tau_{\mathrm{ig}}/\partial C$ are directly evaluated on the FPV manifold. To ensure smoothness of the solution, both Z and C directions are discretized using 500 points. Figure 1a shows the temperature on the FPV manifold. The mixing branch is shown as a dashed gray line. For each of the thermochemical state on this manifold, an isobaric homogeneous reactor calculation is performed using Cantera [26]. The simulations are performed until 10^{-2} s, which is an order of magnitude higher than the experimentally observed autoignition time for the operating conditions

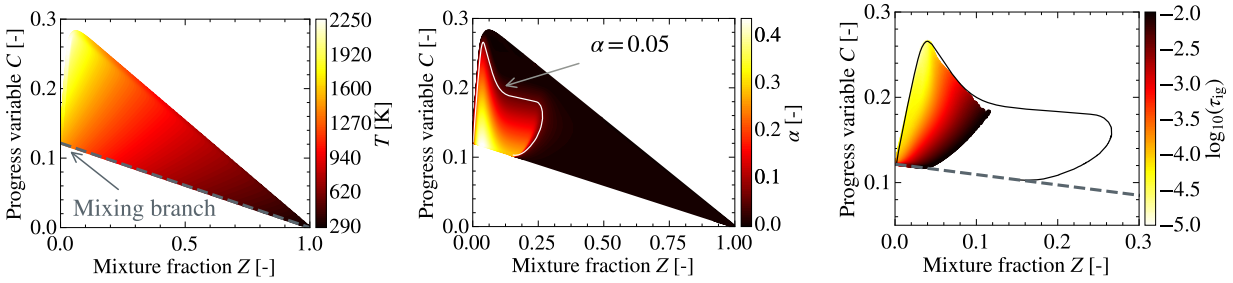

(a) Temperature (b) Heat release parameter (c) Autoignition delay time

Figure 1: FPV-flamelet manifold used for the evaluation of the ignition delay, showing (a) temperature $T_0 = T^{\mathrm{FPV}}(Z, C)$, (b) heat release parameter, $\alpha = (T_f - T_0)/T_f$, and (c) autoignition delay time, $\tau_{\mathrm{ig}}(Z, C)$ [s], computed from an isobaric homogeneous reactor that is initialized with condition from the FPV manifold.

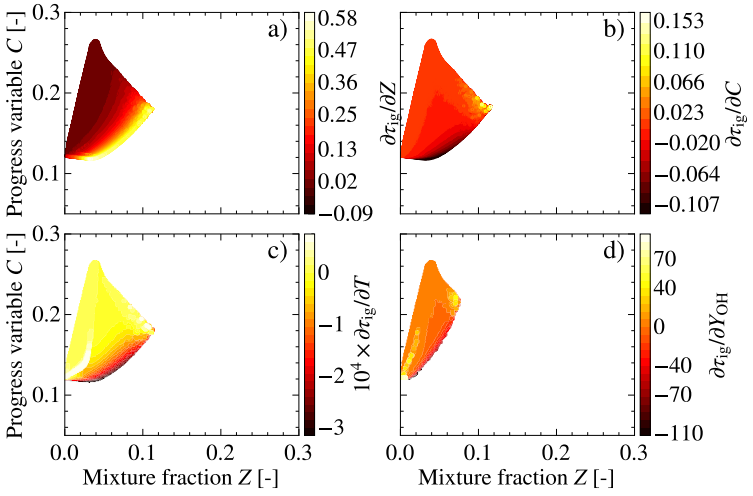

Figure 2: Sensitivity coefficients computed from homogeneous reactor simulation with initial conditions from FPV-flamelet manifold: (a) $\partial\tau_{\mathrm{ig}}/\partial Z$, (b) $\partial\tau_{\mathrm{ig}}/\partial C$, (c) $\partial\tau_{\mathrm{ig}}/\partial T$, and (d) $\partial\tau_{\mathrm{ig}}/\partial Y_{\mathrm{OH}}$.

presented in Sec. 4.1. The autoignition delay time is defined as the time at which the maximum gradient of temperature is reached, namely:

$$\tau_{\mathrm{ig}} = \max \arg_t(d_t T)\,. \tag{11}$$

Other criteria were investigated to assess the robustness of this definition for the autoignition delay time, such as the maximum net production rate of Y_{OH} and Y_{OH^*}. At the most reactive mixture, the most relevant conditions for autoignition for the DLR JHC setup [12] and, more generally, for non-premixed flames [27], these three definitions lead to comparable results for the autoignition delay time as the difference between the maximum and minimum predicted by this criteria is as low as 1.75×10^{-5} s, that is within 2.5% of $\tau_{\mathrm{ig}}(Z_{\mathrm{mr}})$. These HR simulations are initialized with $T_0 = T^{\mathrm{FPV}}(Z, C)$ and reach a final temperature T_f, however, not all compositions lead to ignition. Exothermic conditions are identified using the heat release parameter, $\alpha = (T_f - T_0)/T_f$, which is shown in Fig. 1b. A large region of the flow is endothermic with $\alpha < 0$ or weakly exothermic $\alpha \simeq 0$. Isocontours of $\alpha = 0.05$ are shown in Figs. 1b and 1c. Only values above this threshold – corresponding to a temperature increase of 5.25% with respect to T_0 – are considered ignited,

otherwise the autoignition time is set to $\tau_{\mathrm{ig}} \to \infty$. The autoignition delay time τ_{ig} is shown in Fig. 1c. Values of τ_{ig} on the mixing line are typically on the order of 10^{-3} s. For more complex flames, for instance swirled flames or flames with high levels of recirculation, the ignition conditions may not be as well characterized in the Z-C space than for JHC configurations and it may be necessary to include the entire state-space. The sensitivity coefficients with respect to variations in temperature and OH radicals are determined by performing simulations in which T and Y_{OH} from the FPV-manifold are perturbed. The pre-computed autoignition time is not directly used in the simulation and only employed to evaluate the sensitivity coefficients $\partial\pi/\partial\psi_{\pi,i}$ in Eq. (8). The so computed sensitivity coefficients are shown in Fig. 2.

Since autoignition occurs in regions of low turbulence, we assume that the sensitivity coefficients are statistically independent from $\widetilde{\mathcal{D}}^m_{\psi_{\pi,i}}$. This assumption allows us to simplify the evaluation of the drift term, resulting in the following expression:

$$\widetilde{\mathcal{D}}^m_{\tau_{\mathrm{ig}}} = \sum_{i=1}^{N_\pi} \frac{\partial \tau_{\mathrm{ig}}}{\partial \psi_{\pi,i}} \widetilde{\mathcal{D}}^m_{\psi_{\pi,i}} \ , \tag{12}$$

in which the sensitivity coefficients are tabulated in the FPV chemistry library. It is noted that if Eq. (12) is applied to highly-turbulent environments without revising this assumption, the sensitivity regions would be spatially shifted towards regions of higher turbulence. However, this effect is corrected by modifying the penalty parameter.

4. Experimental configuration and numerical setup

4.1. Experimental configuration

The extended PEC autoignition (PEC-AI) formulation is applied to the DLR-JHC configuration of Arndt et al. [12]. A schematic of the experimental setup is shown in Fig. 3. The fuel is supplied by a central jet of diameter $D = 1.5$ mm surrounded by a vitiated coflow that is supplied through a square section of size 75×75 mm^2. The coflow is provided by a fully premixed lean H_2/air mixture for which the equivalence ratio is modified to obtain different coflow temperatures and compositions.

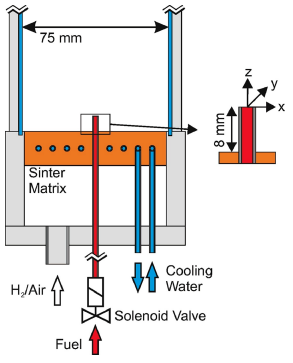

Figure 3: Schematic of the DLR-JHC burner (reproduced from Arndt et al. [12]).

To examine the model sensitivity, the present work considers two operation points, having different temperatures and compositions in the coflow. These conditions are summarized in Table 1. The CH_4 jet is supplied by a pulsed valve to study the stochastic autoignition process. The terminal

bulk velocity of the fuel stream is $U_{\text{bulk}} = 178$ m/s, corresponding to a jet-Reynolds number of 16,000. For both operating conditions studied here, the velocity of the vitiated coflow is 4.1 m/s.

Table 1: Operating conditions of DLR-JHC flame.

Case	Jet	Coflow					
	T [K]	T [K]	X_{N_2}	X_{H_2O}	X_{O_2}	X_{OH}	Z_{st}
TC1490	290	1490	0.712	0.178	0.102	8.20×10^{-5}	0.0279
TC1585	290	1585	0.755	0.130	0.112	1.82×10^{-4}	0.0286

Ignition kernels are identified from measurements of OH* chemiluminescence as described in Arndt et al. [8, 10, 12]. Rayleigh scattering is employed to measure temperature and mixture fraction [11].

The accuracy and spatial resolution of the measurements of mixture fraction and derived temperature are influenced by several effects. In particular, the finite resolution leads to spatial filtering and, thus, possibly to reduced mixture fraction fluctuations as small-scale fluctuations are not fully captured. The laser-light sheet had a thickness of approximately 0.3 mm. Thus, gradients in the normal direction of the laser-light sheet are averaged. This can also lead to an underestimation of the mixture fraction and of mixture fraction fluctuations. Furthermore, the in-plane resolution is limited. The in-plane resolution was determined using an USAF 1951 resolution target with different spatial frequencies. Within the measurement planes, gradients up to 4 mm^{-1} can be resolved. The finite signal-to-noise ratio of the measurements limits the minimum resolvable gradients. Within the coflow ($Z = 0$), mixture fraction gradients larger than 0.2 mm^{-1} can be resolved. In regions with $Z > 0$ smaller gradients can be resolved due to the higher signal-to-noise ratio.

4.2. Numerical setup

The compressible reacting Navier-Stokes equations are solved with the finite-volume solver CharLES$^{\text{x}}$ [21, 28, 29]. A hybrid scheme developed to minimize the numerical dissipation via a blending of fourth-order central scheme and second-order ENO scheme on regular meshes is used. Subgrid-scale (SGS) stresses are modeled by the Vreman eddy-viscosity model [30]. Operator splitting is employed for time integration, in which the non-stiff advection-diffusion operators are solved using a third-order accurate strong-stability preserving Runge-Kutta scheme [31]. To integrate the stiff chemical source terms, a semi-implicit Rosenbrock-Krylov scheme is used, having 4^{th}-order accuracy and linear cost with respect to the number of species [32].

4.2.1. Computational setup

The computational domain considered in this study has a size of $75 \times 75 \times 120$ mm^3 and the coflow inlet is located 8 mm below the jet nozzle exit. The origin is located at the center of the nozzle. The structured mesh contains 5.7 million hexahedral elements with a resolution of $\Delta x = 75\,\mu$m in the injector and the shear layer. The minimum cell size in the flame region is 0.2 mm, which was found to be sufficient to resolve the ignition kernels, having a characteristic length of $l_{\text{ig}} = 1.5$ mm [12]. At the jet inlet, a fully developed turbulent velocity profile with 5% turbulence intensity is imposed using a digital filter technique [33]. The lowest percentage of resolved turbulent kinetic energy, near the nozzle exit, is above 80%, which fulfills the resolution criterion for a reliable LES [34]. Before performing the measurements of the pulsed jet, the H_2/air matrix burner was operated for at least ten minutes, ensuring that all walls have reach thermal

equilibrium [12]. Therefore, the injector lip and the outer walls are modeled by adiabatic no-slip walls.

4.2.2. Combustion modeling

Two submodels are used for the PEC-AI simulations, namely a Finite-Rate Chemistry (FRC) model and the flamelet/progress variable model (FPV). For both models, a reduced CH_4/air mechanism derived by Jaravel et al. [35] is used to which an OH* sub-mechanism [36] is added in order to enable direct comparisons with experimental data. The resulting mechanism has a total of 21 species. A dynamically thickened flame model [37] is used for representing the turbulence-chemistry interaction and constant turbulent Prandtl and Schmidt numbers are used ($\mathrm{Pr_t} = 0.7$ and $\mathrm{Sc_t} = 0.7$) outside of the flame region. Since the flame region is dynamically identified by a flame sensor, this model is not active in regions of autoignition. The maximum thickening factor in the statistically stationary flame is 3 and the maximum efficiency function is lower than 2. The exponent of the efficiency function is kept constant, $\beta = 0.5$. The flame sensor is based on the source term of progress variable to have a consistent subgrid scale turbulence/chemistry interaction closure for all combustion models. The FRC model consists of solving transport equations for all species in the chemical model Eq. (2), with laminar Prandtl and Schmidt numbers different for all species. Contrary to more computationally efficient manifold-based combustion models, detailed FRC models are agnostic to the combustion regime and can, thus, be used to study premixed, non-premixed and autoignition regimes. As such, and similarly to previous PEC studies [21], the FRC model is regarded as the model of highest fidelity in the present work. The thermochemical state in the FPV model is obtained from the solution of steady flamelets along the S-curve, including the unstable branch. To avoid inconsistencies due to preferential diffusion effects, mixture fraction is transported throughout the entire domain [21]. A first order approximation of the relative costs of the combustion models can be obtained from the number of transported scalars. As only two scalars are transported for FPV, the current FRC model should computationally more expensive by an order of magnitude. However, computational overhead associated with the evaluation of the drift-term, application of boundary conditions, and dynamic submodel assignment require consideration.

4.2.3. Transient injection conditions

To capture the correct ignition time, the transient injection has to be accurately modeled. For this, we follow the work by Inanc and Kempf [15] and model the transient injection by a linear ramp. Papageorge et al. [11] estimated the initial velocity of the jet to be between 40 and 50 m/s. Therefore, an initial bulk velocity of 45 m/s was used and the duration of the transient injection is set to 0.4 ms. A fully developed turbulent velocity profile is imposed in the injector (fuel inlet) by prescribing the mean and RMS fluctuations. The ramping strategy is implemented by scaling the mean and RMS profiles in time and the results are presented in Fig. 4. Figure 4a shows the temporal evolution of the scaled "mean" target velocity profile at the center of the injector nozzle ($\boldsymbol{x} = \mathbf{0}$) by the dashed blacked line. A typical axial velocity signal recorded at the origin from a FPV simulation is shown by the gray solid line and referred to as "Probe" in Fig. 4a. This ramping strategy is assessed by comparing the jet penetration length obtained from monolithic FRC and FPV simulations and PEC-AI with measurements reported by Arndt et al. [12]. The jet penetration length is computed from an isocontour of mixture fraction, $x_{\mathrm{JPL}} = \max(x \mid Z > Z_\Theta)$ where, consistently with [12], the threshold value is set to $Z_\Theta = 0.1$, approximately three times the stoichiometric value. As shown in Fig. 4b the results obtained for

the jet penetration length compare favorably with measurements [12] and the combustion models (monolithic FRC, monolithic FPV and PEC-AI with a penalty term of $\lambda = 10^{-4}$) do not have an appreciable effect on the transient jet dynamics during the injection phase.

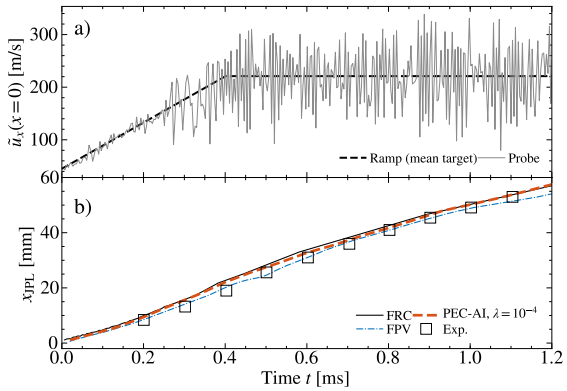

Figure 4: a) Transient injection and b) jet penetration length.

5. Results

In this section, results from PEC-AI simulations and comparisons with monolithic FRC and FPV simulations are presented for two operating conditions. To examine the performance of PEC-AI in predicting lift-off and transient ignition dynamics, we first consider the Case TC1490 (see Table 1), for which a detailed set of measurements is available. The sensitivity of PEC-AI in predicting effects of variations in the coflow temperature is examined by considering the Case TC1585, having a higher coflow temperature and reduced lift-off height. To demonstrate the merit of the PEC-AI formulation, comparisons with 1) the previously developed PEC-formulation (denoted by PEC-C) are performed, in which the drift term was defined using the set of QoIs, $Q = \{Y_{\mathrm{CO}}, Y_{\mathrm{CO_2}}, Y_{\mathrm{H_2O}}, Y_{\mathrm{H_2}}\}$ [21] and 2) a PEC-formulation (denoted PEC-C-OH) that also includes OH, which was identified as species that affects the autoignition time, $Q = \{Y_{\mathrm{CO}}, Y_{\mathrm{CO_2}}, Y_{\mathrm{H_2O}}, Y_{\mathrm{H_2}}, Y_{\mathrm{OH}}\}$.

5.1. Influence of penalty parameter

As discussed in Sec. 2, the penalty parameter λ allows to balance accuracy and cost of the PEC-AI simulation. Changing this parameter leads to a change in submodel assignment as well as a change in the cost and the error of the simulation. Since the error is dependent on the flow-field, the FRC-utilization will be dynamically adjusted during the transient simulation according to the user-prescribed value of λ. In this section, the effect of this parameter on the cost and the error of the combustion model is examined. The global error is defined from the model mapping as presented in Eq. (4). From the definition of the drift term (Eq. (6)), it is clear that, since FRC is considered the model of highest fidelity, if the entire computational domain is assigned to FRC, $\mathcal{M}(\boldsymbol{x}) = m_2$, the global error is $\mathcal{E}_{\mathrm{FRC}} = 0$. Conversely, assigning the entire computational domain to FPV, $\mathcal{M}(\boldsymbol{x}) = m_1$, results in the maximum global error $\mathcal{E}_{\mathrm{FPV}}$.

We noted that during the transient ignition process the error grows from a zero value since the initial mixing state is accurately captured by the FPV model. When the flame reaches a stationary state, the error converges to a stationary value that fluctuates due to the turbulent flow field.

To study the effect of λ on the submodel assignment, a series of simulations is performed in which λ is changed over a wide range of conditions. The corresponding FRC-submodel utilization as a function of λ is shown in Fig. 5. These simulations are performed for one time-step after the flame has reached a statistically stationary state. From the results, shown in Fig. 5, it can be

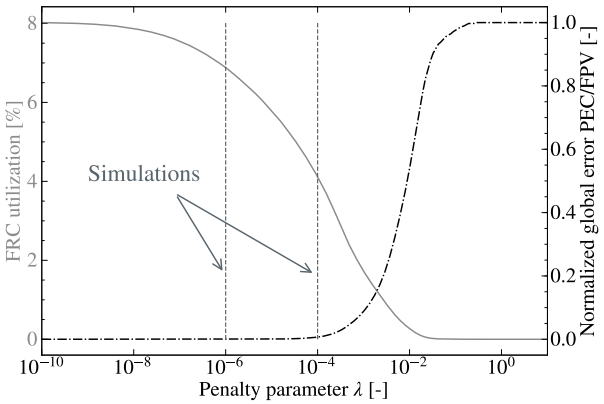

Figure 5: Percentage of control volumes utilizing FRC and resulting normalized error $\mathcal{E}_{\mathrm{PEC}}(\lambda)/\mathcal{E}_{\mathrm{FPV}}$ as a function of the penalty parameter λ.

seen that for values of λ above 10^{-1} the monolithic FPV model is recovered. While in previous investigations [19, 20, 21], the monolithic FRC model was recovered (100% FRC utilization), in the present study, PEC-AI attains a maximum FRC-utilization of 8% in the limit of $\lambda \to 0$. This is due to the definition of the drift term for autoignition: in large regions of the flow, corresponding to the coflow, the burnt products and the fuel, the thermochemical state is insensitive to the ignition delay. Regions of the flow where the thermochemical state may lead to autoignition is, thus, only defined in a small fraction of the computational domain, here only 8%, which demonstrates the selectivity of the current drift term formulation. Finally, a λ-value of 10^{-3} leads to an error level of 10% of the monolithic FPV simulation for about 2% of FRC utilization.

In the following, simulations with two different λ-values are performed, namely $\lambda = 10^{-4}$ and $\lambda = 10^{-6}$ leading to a FRC-utilization of about 3.5% and 7%, respectively.

5.2. Comparison of PEC-model assignment

Figure 6 shows instantaneous fields before (A, $t = 1.9$ ms) and after ignition (B, $t = 3.2$ ms). The λ parameters for PEC-C ($\lambda = 3 \times 10^{-2}$) and PEC-AI ($\lambda = 10^{-4}$) are chosen such that both simulations have a comparable FRC-utilization of 4% at statistically stationary conditions.

As shown in Fig. 6A-1 and Fig. 6B-1, the mixture fraction fields are comparable for the two PEC formulations, before and after ignition. Before ignition (Fig. 6A-2), both PEC formulations show similar temperature fields and the cold turbulent fuel jet (gray) is mixing with the hot coflow (white). At this stage, the coherent mixture fraction and temperature fields indicate that the flow is controlled by turbulent mixing. After ignition (Fig. 6B-2), a discrepancy between temperature fields is observed. In particular, the two models predict a different flame lift-off height h_{LO}, visualized by the lowest axial position of the regions hotter than the coflow (red). In this work, the lift-off height h_{LO} is defined as the minimum axial location for which the temperature is higher or equal to a threshold θ_{LO}, that is $h_{\mathrm{LO}} = \min \arg_x(T(x) \geq \theta_{\mathrm{LO}})$, with $\theta_{\mathrm{LO}} = 1560$ K. This temperature threshold corresponds to a 5% temperature increase with respect to the coflow temperature,

typically used to visualize the temporal evolution of ignition kernels [12]. It is noted that this quantity is highly unsteady such that the values indicated are qualitative; a quantitative analysis of time-averaged profiles is performed in Fig. 8. The discrepancy in h_{LO} is explained by the submodel assignments, as shown in Fig. 6A-3 and Fig. 6B-3, as the two drift term formulations produce significantly different local submodel assignments. The isocontour of temperature corresponds to an increase of 5% with respect to the coflow temperature. Before ignition, PEC-C uses FRC in the core of the jet while PEC-AI assigns FRC in the shear layer and around the most reactive mixture fraction Z_{mr}. Steady flamelet models have been shown to under-predict h_{LO} [5, 15]. For PEC-C, the flame root and Z_{mr} are located in FPV regions, which explains the under-prediction of h_{LO}. Conversely, PEC-AI detects these regions and assigns them to the FRC submodel. Finally, as expected, the burned product regions are computed by FPV and small isolated ignition kernels are assigned to FRC.

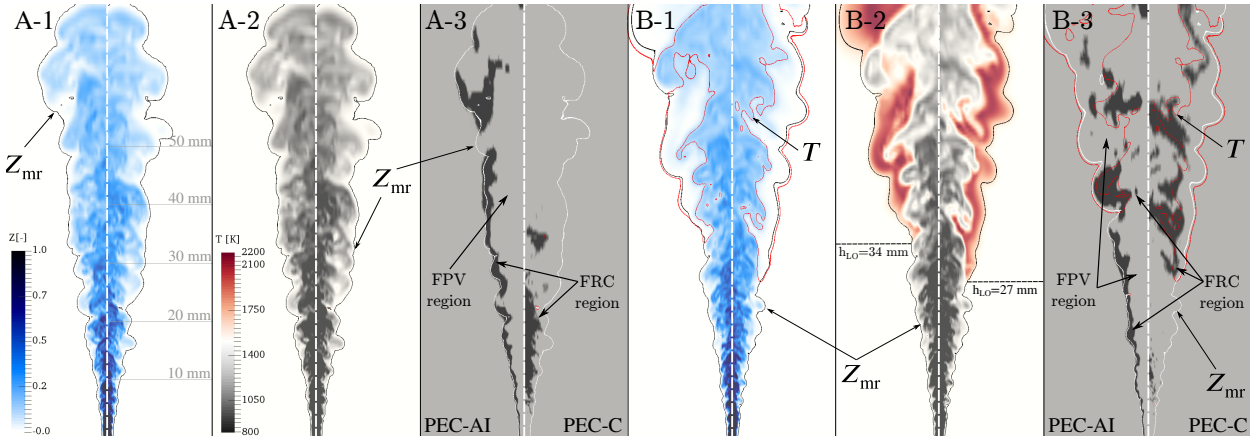

Figure 6: Instantaneous fields of (1) mixture fraction, (2) temperature and (3) submodel assignment (A) before and (B) after ignition. Panels on the left and right correspond PEC-AI ($\lambda = 10^{-4}$) and PEC-C, respectively. The FRC regions are in black and FPV regions in grey. Isocontours of temperature ($T = 1560$ K) and most reactive mixture fraction are shown. The axial locations of the radial profiles are shown. Results are shown for Case TC1490.

5.3. Stationary operating condition

5.3.1. Time-averaged profiles

Figure 7 shows centerline profiles of CH_4 mass fraction and temperature averaged over 7.5 ms, corresponding to 890 flow time scales based on the bulk velocity and the diameter of the fuel injector. All models show good agreement with the measurements. It is noted, that FRC performs better than FPV, especially for the temperature far from the nozzle exit, and this trend is accurately reproduced by the PEC-AI simulation. The computational costs of the monolithic FPV and FRC submodels (Table 2) are 1150 and 12500 CPUh per millisecond of physical time. The PEC calculations lead to a cost of 4810 and 5040 CPUh/ms for the penalty parameters of $\lambda = 10^{-4}$ and $\lambda = 10^{-6}$, that is 38% and 40% of the computational cost of the monolithic FRC simulation, using dynamic load rebalancing [32]. Computational overhead arises from the computation of the drift term, the evaluation and exchange of boundary conditions at the submodel interfaces, and the source term evaluation in spatially inhomogeneous subdomains. Two methods were used to estimate this overhead. First, the overhead can be expressed from the cost scaling of a PEC simulation, $C_{\mathrm{PEC}} = f_{\mathrm{FRC}} C_{\mathrm{FRC}} + (1 - f_{\mathrm{FRC}}) C_{\mathrm{FPV}} + C_{\mathrm{overhead}}$ where f_{FRC} is the fraction

of control volumes assigned to FRC and C_{overhead} denotes the computational overhead. From the aforementioned computational cost, the overhead for the two PEC simulations is 24% and 25% of the monolithic FRC simulation. The second method consists in using a very large value for the penalty parameter, here $\lambda > 1$ (see Fig. 5), to evaluate the cost of a simulation with 0% FRC utilization. With this method, the overhead is determined to be 28% of the cost of the monolithic FRC simulation.

Table 2: Computational cost and FRC utilization for monolithic and PEC-AI simulations at statistically stationary conditions.

	FRC	FPV	PEC-AI ($\lambda = 10^{-4}$)	PEC-AI ($\lambda = 10^{-6}$)
Computational cost [CPUh/ms]	1150	12500	4810	5040
FRC utilization (stationary conditions) [%]	100	0	3.5	7.0

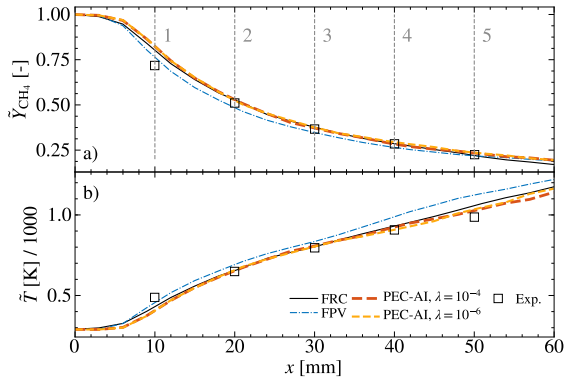

Figure 7: Comparison of centerline profiles for (a) mean CH_4 mass fraction and (b) temperature for PEC-AI, FPV, FRC and experimental data for the case TC1490.

Figure 8 shows a comparison of radial profiles of the mean and RMS results at five axial locations (shown in Fig. 6A-1 and Fig. 7). The statistical results for PEC-AI are compared with monolithic FRC and FPV simulations and measurements. The experimental radial profiles are binned into regular intervals and the mean value is represented as a solid black line. The experimental uncertainties are not represented in Fig. 7 and the minimum and maximum values within each interval are reported as vertical bars. The mean temperature and $\widetilde{Y}_{CH_4}$ profiles of FRC are in good agreement with experimental results for all axial locations, indicating that the flame stabilization and h_{LO} are well captured. The flame spreading angle for the stationary flame, visualized by the radial location of the maximum temperature, is also correctly predicted by FRC. The monolithic FPV simulations under-predict h_{LO}, resulting in a large discrepancy for temperature profiles and spreading angle. It is noted that the statistically stationary results of the compressible flamelet formulations used in [15] (not shown here) predict a h_{LO} closer to the measurements compared to the monolithic FPV. However, the mean and RMS profiles of temperature at $x = 40$ mm and $x = 50$ mm are comparable to the monolithic FPV: the maximum measured temperature at $x = 40$ mm is 1500 K and the maximum predicted temperature are: 1950 K for the monolithic FPV, 1600 K for the approaches used by [15], and 1580 K for the monolithic FRC. The probability of the dynamic PEC-AI model assignment (for $\lambda = 10^{-6}$) is shown in Fig. 8 in the form of a colormap. A probability of 0% corresponds to regions where FPV is always used and 50% to regions where FRC is assigned half

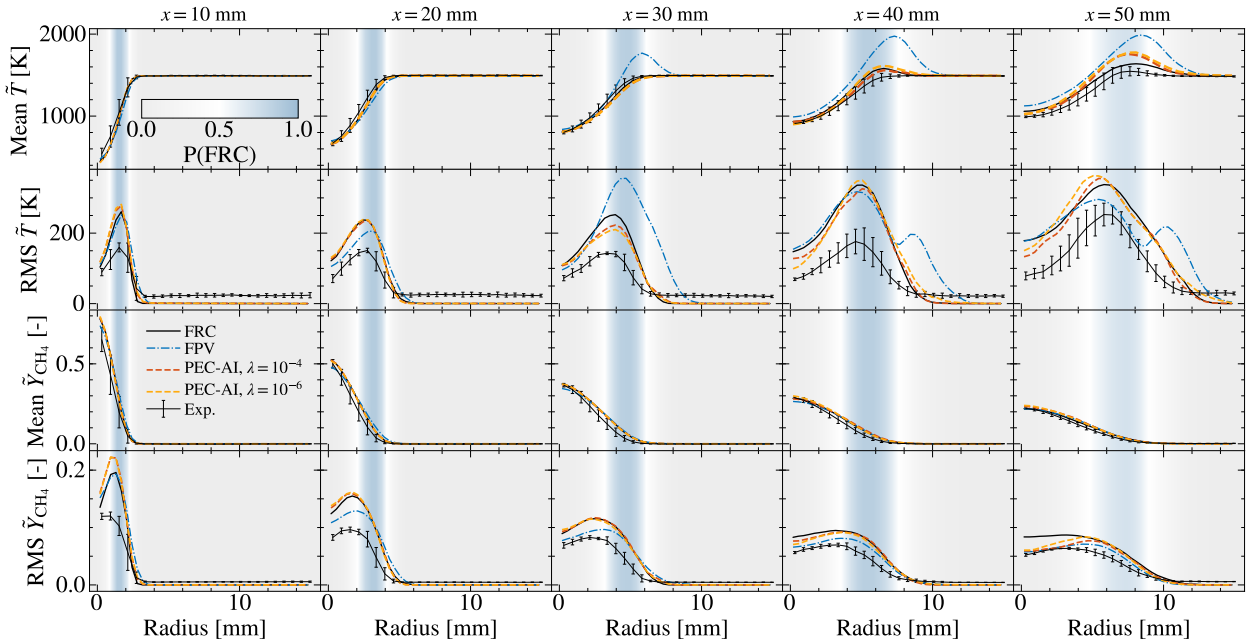

Figure 8: Radial profiles of temperature and CH_4 mass fraction and probability of model assignment for case TC1490 at five axial locations (cf. Fig. 6) for FRC, FPV, PEC-AI and experimental results [2].

of the time. Both PEC-AI simulations show similar profiles and are able to retrieve the mean FRC profiles and, thus, the correct spreading angle and h_{LO}. The RMS quantities are over-predicted for all simulations, indicating that the flame root is predicted to be more unsteady compared to the experiment. RMS over-predictions, especially for temperature profile, have also been observed by [14, 15] on the same operating conditions. As the flame stabilization is very sensitive to coflow conditions, these differences may appear due to uncertainties in the coflow mass flow rate (of the order 1-1.5%) and, mostly, in the coflow temperature due to a lower signal-to-noise ratio in this region [12]. This is visible in Fig. 8 as the experimental RMS of temperature in the coflow is of the order of 25 K at all axial locations. Nonetheless, PEC-AI retrieves profiles in good agreement with FRC, even in regions where only FPV predicts a flame, e.g. $x = 30$ mm, which can be attributed to the fact that FRC is assigned to the flame root (see Fig. 6 for submodel assignment). Since FRC is considered to be the model of highest fidelity, PEC-AI cannot yield more accurate results that the monolithic FRC. The probability of locally assigning FRC reduces with downstream distance, as this region of the flow is well described by the FPV model and the selective drift term sensor becomes inactive.

Overall, PEC-AI is capable of retrieving the FRC profiles in regions of interest with only 3.5% of FRC submodel assignment in the domain for $\lambda = 10^{-4}$ and decreasing the penalty parameter does not lead to a significant improvement in this case.

5.3.2. Comparison with QoI-based drift term formulation

The time-averaged results of the PoI-based drift term formulation introduced in Sec. 3 have been analyzed. However, only qualitative comparisons have been conducted so far. Here, we perform a quantitative comparison between the current PoI formulation and two QoI-based drift term formulations. The first formulation is the PEC-C (see Sec. 5) for which the set of QoIs is

defined as $Q = \{Y_{CO}, Y_{CO_2}, Y_{H_2O}, Y_{H_2}\}$. This formulation has been used in previous studies using the PEC framework [21].

From the sensitivity analysis that was performed to identify the scalar dependencies ψ_π of the surrogate π, the most sensitive quantity has been identified to be Y_{OH}. Adding this species to the set of QoIs may have a strong impact on the solution with minimum changes to the methodology of [19]. Hence, the second formulation, denoted as PEC-C-OH, uses the following set of QoIs, $Q = \{Y_{CO}, Y_{CO_2}, Y_{H_2O}, Y_{H_2}, Y_{OH}\}$.

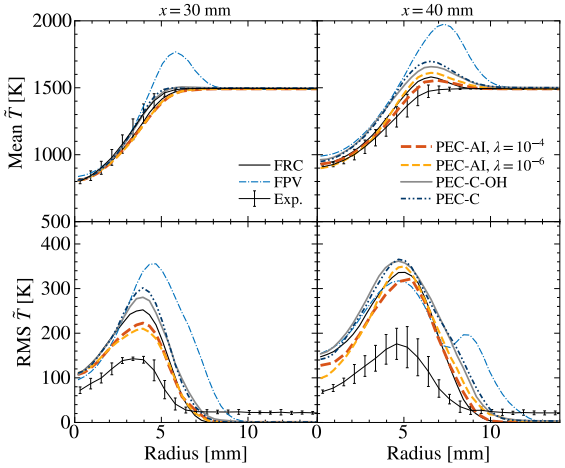

Figure 9: Comparison of radial time-averaged temperature profiles for two PoI-based drift term formulations (PEC-C and PEC-C-OH), the PoI formulation ($\lambda = 10^{-4}$ and $\lambda = 10^{-6}$) and the monolithic FRC and FPV simulations for case TC1490.

Figure 9 shows time-averaged radial temperature profiles for PEC-C and PEC-C-OH at $x = 30$ and $x = 40$ mm for the case TC1490. As in Fig. 8, these profiles are the most relevant as they are located upstream and downstream of the experimentally observed flame root. In Fig. 9, the measurements are reported for reference. However, the comparison of the proposed PEC formulations should be performed with respect to the monolithic FRC profiles, since the highest-fidelity PEC formulation is acheived for $\lambda = 0$, which corresponds to a maximum FRC utilization. Both QoI-based formulations yield improved predictions of the statistically stationary state in comparison to the monolithic FPV simulation. In particular, the mean flame lift-off height is closer to the monolithic FRC. However, as shown in Fig. 6, for PEC-C the shear layer is assigned to the FPV model and a very similar submodel assignment is obtained for PEC-C-OH (not shown here). This results in a misprediction of the spreading angle, in particular near the centerline ($r < 4$ mm), where the spreading angle predicted by FPV is retrieved by both QoI-based PEC-formulations. At $x = 40$ mm, the radial profiles of time-averaged temperature show that the mean temperature peak is overpredicited by PEC-C and PEC-C-OH. In addition, the radial locations of these peaks are slightly shifted towards the coflow region. As expected, the addition of Y_{OH} to the set of QoIs allows to improve the prediction of the flame lift-off height, as shown by the reduced peak temperature of PEC-C-OH at $x = 40$ mm with respect to the PEC-C results.

Even though, Fig. 9 demonstrates that the addition of Y_{OH} to the QoI has a marginal effect on the statistically stationary temperature profiles, this formulation does not improve the prediction of the autoignition time and location due to a submodel mapping similar to the PEC-C formulation (Fig. 6).

5.3.3. Sensitivity to coflow temperature

We proceed by examining the capability of the PEC-AI formulation in predicting effects of variations in the coflow temperature on the lift-off height. To this end, additional simulations with a coflow temperature of 1585 K (Case TC1585, see Table 1 for coflow composition) are conducted, corresponding to the highest coflow temperature for which radial measurements at $x = 30$ mm are available [2].

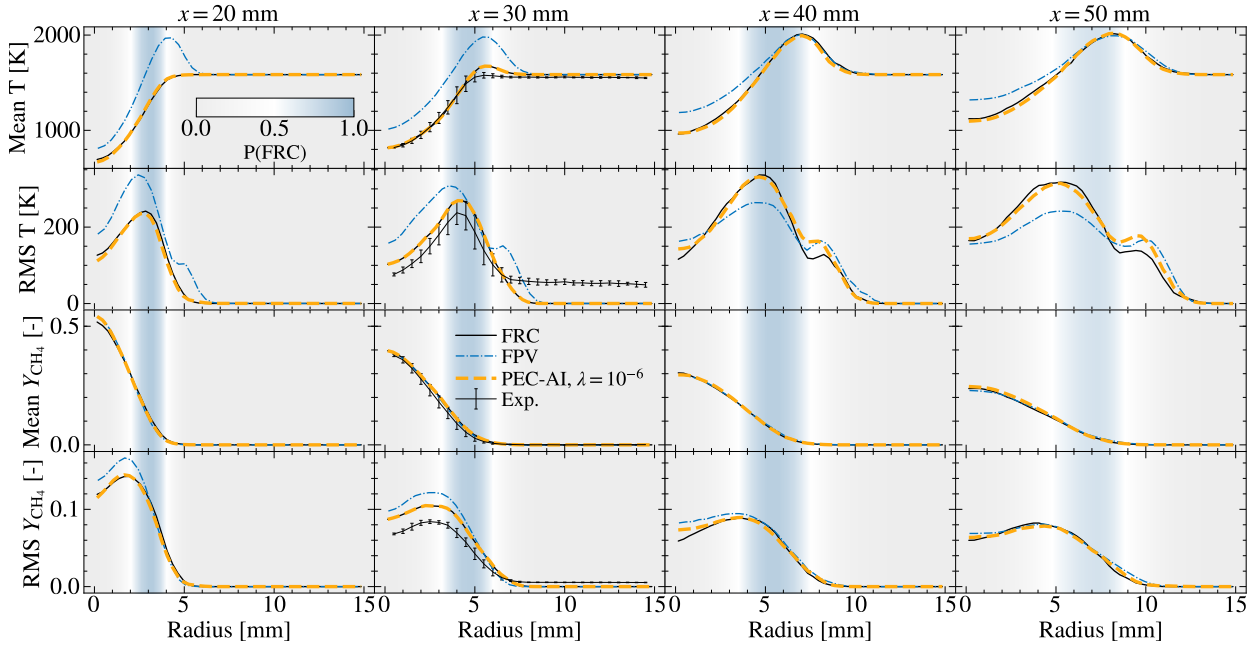

Figure 10: Time-average radial profiles for monolithic FRC, monolithic FPV, PEC-AI ($\lambda = 10^{-6}$) and measurements for case TC1585.

Figure 10 shows mean and RMS profiles of temperature and methane mass fraction. Although Arndt et al. [2] reported a coflow temperature of $T_c = 1585$ K, the radial profile at $x = 30$ mm indicates that the coflow temperature is about 25 K below the nominal value. The large RMS temperature in the coflow suggests that the boundary conditions exhibit a higher level of unsteadiness compared to the case TC1490. For this high-temperature coflow condition, the temperature measurements show that the location of the flame root is highly unsteady and is located around $x = 30$ mm, as shown by the peak location in the mean temperature profiles and the high RMS values at $r = 5$ mm. FPV grossly under-predicts the flame root location as shown by the temperature peak for $x = 20$ mm. In contrast, the monolithic FRC simulation predicts a slightly higher temperature, indicating that the location of the flame root is under-predicted, which is consistent with the results obtain for the coflow temperature $T_c = 1490$ K and the discrepancy between the measured and nominal coflow temperature [2]. Both FPV and FRC simulations predict the same spreading angle as the radial peak-temperature location are the same at $x \geq 30$ mm. Results for the PEC-AI simulation with $\lambda = 10^{-6}$ show that the spreading angle of the FRC simulation is recovered as well as the temperature and methane profiles. Some small discrepancies between FRC and PEC-AI are observed in the upper part of the flame at $x = 40$ mm and $x = 50$ mm, corresponding to regions with a very low probability of FRC utilization.

5.4. Transient ignition dynamics

To assess the capability of PEC-AI to capture stochastic autoignition, ensemble simulations are conducted and the autoignition time τ_{AI}, the ignition height h_{AI} and the radial position r_{AI} of the ignition kernels are recorded from which probability distributions P are computed. Variability is introduced in each simulation by randomly seeding the inflow conditions of individual simulations for all combustion models, namely, FPV, FRC, PEC-AI ($\lambda = 10^{-4}$) and PEC-AI ($\lambda = 10^{-6}$).

5.4.1. Dynamic submodel assignment in PEC-AI

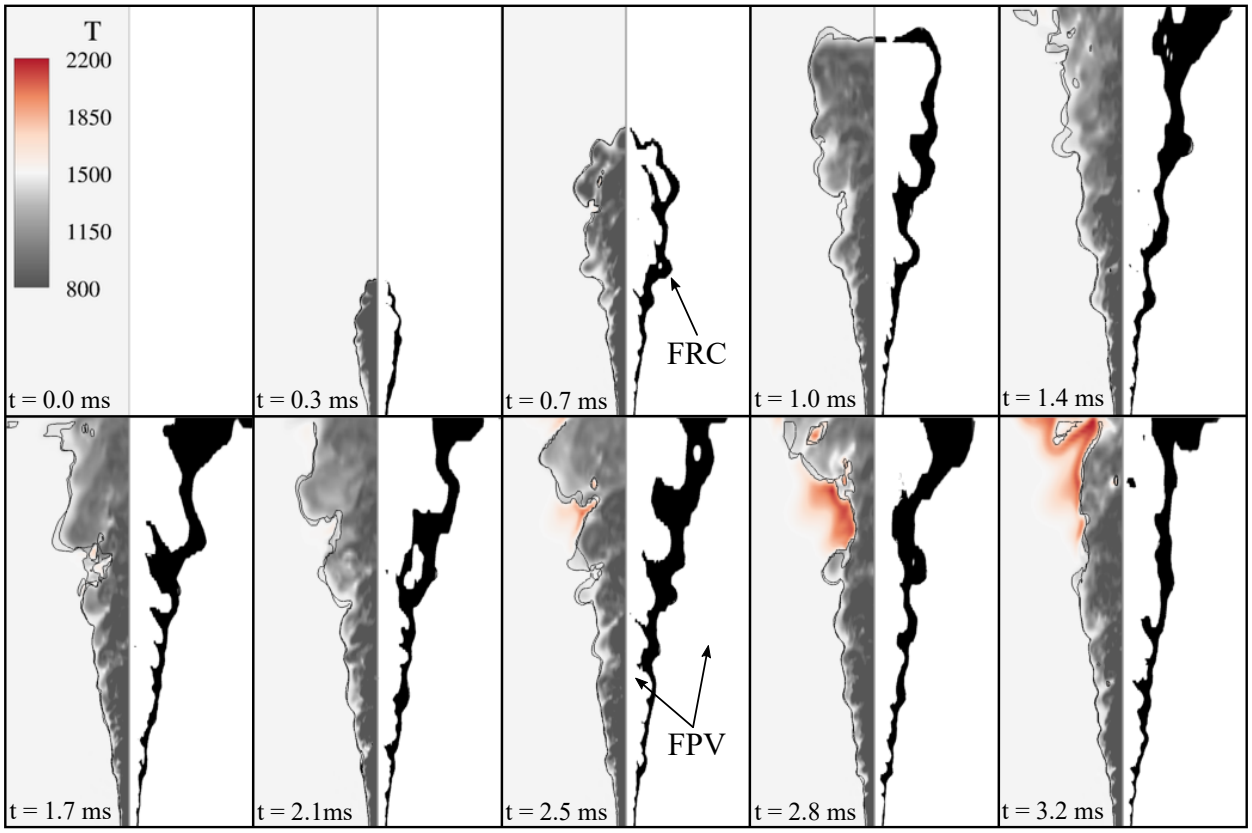

Figure 11: Dynamic submodel assignment, showing (left) instantaneous temperature (in K), and submodel assignment fields (right) obtained during the transient ignition simulation for PEC-AI ($\lambda = 10^{-6}$) for case TC1490. The nozzle exit coincides with the bottom of the figure.

Figure 11 shows instantaneous results for temperature and submodel assignment obtained during a transient simulation for PEC-AI ($\lambda = 10^{-6}$) for case TC1490. At the initial condition ($t = 0$ ms) the thermochemical state is fully described by inert mixing. For this condition, the PEC-AI submodel assignment is prescribed by a uniform FPV utilization. At later times ($0 < t < 2.1$ ms) the mixing layer develops and discrepancies between the thermochemical states predicted by FRC and FPV appear, which results in a finite drift term. In accordance, the region of FRC utilization expands in time and is dynamically adjusted and localized around the most reactive mixture. At $t = 0.7$ ms, the ejection of a fuel-rich pocket into the high-temperature coflow is observed. Small autoignition kernels appear in this region at $t = 1.7$ ms at the most reactive mixture. However, these autoignition kernels rapidly extinguish by turbulent mixing, as shown by the temperature

field at $t = 2.1$ ms. Eventually, sustainable ignition is observed at $t = 2.5$ ms, resulting in the successful transition to a stably burning flame.

Figure 12 shows the temporal evolution of the FRC utilization for 20 ensemble simulations performed for PEC-AI ($\lambda = 10^{-6}$). All simulations are initialized with the FPV-model at $t = 0$ s. With the development of the mixing layer (see Fig. 11) the FRC utilization increases as a consequence of the detected deficiency in the FPV-model compliance with the flow-field representation. Although the submodel assignment for all simulations is similar, differences in the initial conditions lead to a separation of the flow-field solution. This separation evolves on a time that scales with the integral time and can be related to the Lyapunov exponent [38]. According to user-specific requirements on the solution accuracy (expressed through the selected value of λ), the dynamic submodel assignment changes, which is illustrated in Fig. 12 by the spread of the FRC utilization during the simulation. The ensemble averaged FRC utilization at the time of autoignition, visualized by the experimental PDF of τ_{AI} in Fig. 12, is 4.5%. In comparison, the maximum FRC utilization for PEC-AI ($\lambda = 10^{-4}$), obtained in the stationary flame (Fig. 5), is 3.5% and the ensemble average FRC utilization at the time of autoignition (not shown here) is only 2%.

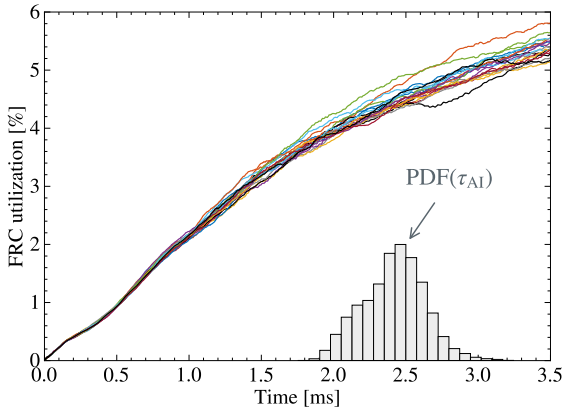

Figure 12: Temporal evolution of the FRC utilization during the ignition phase for 20 separate ensemble simulations for PEC-AI ($\lambda = 10^{-6}$) and experimental PDF of autoignition time [12]. Results are presented for case TC1490.

5.4.2. Prediction of stochastic ignition dynamics

Following the experimental procedure of Arndt et al. [12], ignition kernels are identified from thresholding the OH* mass fraction and a level of 10^{-12}, corresponding to 50% of the maximum value, is used. Due to the sudden temporal evolution of $\widetilde{Y}_{\mathrm{OH}^*}$, the choice of the threshold value was found to only have a marginal effect on τ_{AI}, h_{AI} and r_{AI} [24].

To compare the stochastic values of τ_{AI}, h_{AI} and r_{AI} predictied by each model, it is necessary to evaluate the required sample size, that is, the number of simulations needed. Due to the computational burden associated to LES calculations, especially for the monolithic FRC, this sample size should be kept as low as possible. Here, the minimum sample size requirement is verified *a posteriori* by analyzing the convergence of the cumulative mean and standard deviation of τ_{AI}, h_{AI} and r_{AI} (not show here) as the samples are collected. This is shown in Fig. 13 for each of the considered combustion models. The standard deviation σ of a given Gaussian distribution is reported as a range around the mean value, $\mu \pm k\sigma$, where μ denotes the mean and k is chosen to be $k = 0.125$, such that 25% of the ignition events fall within the reported ranges of τ_{AI} and

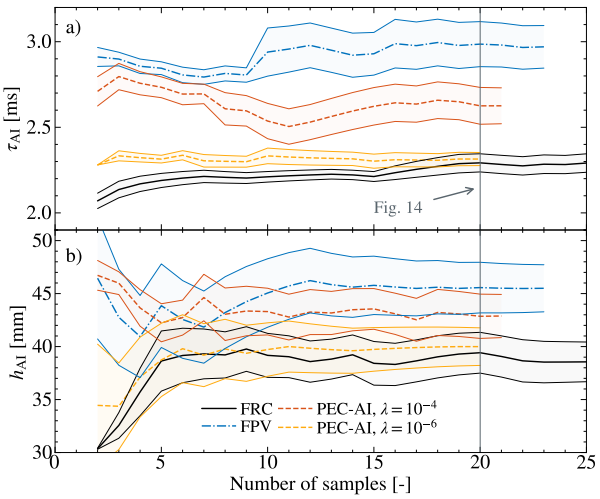

Figure 13: Convergence of the mean and standard deviation as a function of the number of collected samples for the monolithic FRC, the monolithic FPV and PEC-AI ($\lambda = 10^{-4}$ and $\lambda = 10^{-6}$) simulations. Results are presented for the case TC1490.

h_{AI}. Even though large variations of the cumulative mean and standard deviations are visible for less than 10 samples, the orders of magnitude of these quantities are well established for all models with approximately 15 samples. Although small variations are still present, the differences between the considered models is statistically significant. As shown in Fig. 13, the value of 20 samples is sufficient to obtain the stochastic quantities of the different combustion models with reasonable accuracy.

The mean and standard deviation obtained for each model are compared with the measurements for the case TC1490 in the form of a Gaussian distribution in Fig. 14 after collecting 20 samples. This comparison shows that the obtained predictions from the monolithic FRC simulation are

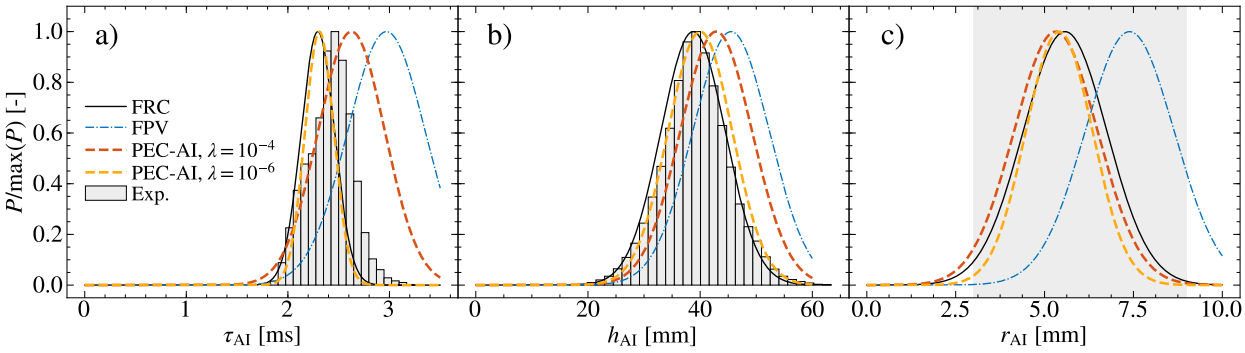

Figure 14: Normalized distributions for ignition time, height and radius for PEC-AI, monolithic FRC and FPV simulations and the measurements. The shaded area corresponds to the range reported by [12]. Results are presented for case TC1490.

in satisfactory agreement with measurements. h_{LO} is well predicted, τ_{AI} is shifted by 0.2 ms ($< 5\%$) and the radial location r_{AI} falls within the experimentally observed range [12]. This result confirms that the consideration of inlet turbulence is adequate to reproduce the distribution of the measured quantities. In contrast, monolithic FPV simulations significantly over-predict these

quantities, which was also observed by Inanc and Kempf [15] for other steady-state flamelet-based combustion models. This can be attributed to the fact that steady flamelet models do not account for the transient ignition, which is controlled by the initial development of a radical pool [5].

PEC-AI results are within the values predicted by FRC and FPV. Using a penalty term of $\lambda = 10^{-4}$, the predictions of the ignition delay are improved over FPV simulations with average relative errors of the mean τ_{AI} of 14% and 30% compared to the prediction of FRC and FPV, respectively.

Decreasing the value of the penalty parameter to $\lambda = 10^{-6}$, leading to a larger FRC utilization, significantly improves the accuracy for predicting the transient ignition. For all quantities, τ_{AI}, h_{AI} and r_{AI}, PEC-AI ($\lambda = 10^{-6}$) is able to generate results that are comparable to FRC results at reduced cost and a substantially lower FRC-submodel assignment that does not exceed 5% of the computational domain. These results demonstrate that regions necessary for predicting transient ignition dynamics are successfully identified by the novel drift term formulation for autoignition.

6. Conclusions

In this study, the PEC framework is extended to predict the autoignition in turbulent flames. To this end, the drift-term formulation is extended to consider processes of interest by introducing the ignition delay of an isobaric homogeneous reactor as surrogate for the autoignition. A sensitivity analysis is performed to identify parametric dependencies of ignition delay to thermochemical quantities, consisting of temperature, mixture fraction, progress variable and OH mass fraction.

The resulting PEC-AI formulation is applied to the DLR-JHC configuration and two different operating conditions are considered. FRC and FPV are used as submodels for the PEC-AI simulations. Monolithic FRC simulations are performed to demonstrate the capability of accurately modeling transient ignition features and lift-off height. Comparisons with monolithic FPV simulations show significant mispredictions of ignition time and flame lift-off of the FPV model. The extended PEC-AI formulation dynamically identifies deficiencies of the FPV model and locally assigns the FRC submodel in regions of the most reactive mixture composition. An analysis of the submodel assignment and the performance of the PEC-AI formulation is performed, showing that the FRC accuracy is recovered using less that 5% FRC-utilization in the computational domain. The computational cost for the PEC-AI simulation was less than 40% of that of a monolithic FRC simulation. The PEC overhead arising from the computation of the drift term, application of boundary conditions at submodel interfaces, and the source term evaluation is approximately 25% and further improvements are achievable using subzone lumping and more efficient domain partitioning.

The transient autoignition process is studied by performing ensemble simulations and distributions of ignition time, height and radial locations of the ignition kernels are reported. It is shown that the utilization of PEC-AI improves the solution accuracy by targeting deficiencies of the FPV combustion model. The effect of the level of FRC utilization is shown by conducting two sets of ensemble calculations with two values for the penalty parameter. Although statistically stationary conditions were in agreement with measurements, a penalty parameter of $\lambda = 10^{-6}$ was found to be necessary to accurately capture the transient ignition processes, resulting in 4.5% FRC utilization at the time of ignition. This PEC-AI simulation of highest fidelity was found to fully recover the FRC-results at significantly reduced cost.

This study illustrates the ability of the PEC formulation in targeting different combustion

response functions that include not only species and emissions but also transient combustion processes.

Acknowledgments

This work was supported by NASA Award #NNX15AV04A and AFOSR with Award #FA9300-19-P-1502. Computational resources were provided by NASA High-End Computing (HEC) Program through NASA Advanced Supercomputing (NAS) Division at Ames Research Center.

References

[1] F. Güthe, J. Hellat, P. Flohr, The reheat concept: The proven pathway to ultralow emissions and high efficiency and flexibility, J. Eng. Gas Turb. Power 131 (2009) 641–648.

[2] C. M. Arndt, M. J. Papageorge, F. Fuest, J. A. Sutton, W. Meier, Experimental investigation of the auto-ignition of a transient propane jet-in-hot-coflow, Proc. Combust. Inst. 37 (2019) 2117–2124.

[3] R. Cabra, T. Myhrvold, J. Y. Chen, R. W. Dibble, A. N. Karpetis, R. S. Barlow, Simultaneous laser Raman-Rayleigh-LIF measurements and numerical modeling results of a lifted turbulent H2/N2 jet flame in a vitiated coflow, Proc. Combust. Inst. 29 (2002) 1881–1888.

[4] P. Domingo, L. Vervisch, D. Veynante, Large-eddy simulation of a lifted methane jet flame in a vitiated coflow, Combust. Flame 152 (2008) 415–432.

[5] M. Ihme, Y. C. See, Prediction of autoignition in a lifted methane/air flame using an unsteady flamelet/progress variable model, Combust. Flame 157 (2010) 1850–1862.

[6] O. Schulz, T. Jaravel, T. Poinsot, B. Cuenot, N. Noiray, A criterion to distinguish autoignition and propagation applied to a lifted methane-air jet flame, Proc. Combust. Inst. 36 (2017) 1637–1644.

[7] C. M. Arndt, W. Meier, Influence of boundary conditions on the flame stabilization mechanism and on transient auto-ignition in the DLR jet-in-hot-coflow burner, Flow Turbul. Combust. 102 (2019) 973–993.

[8] C. M. Arndt, J. D. Gounder, W. Meier, M. Aigner, Auto-ignition and flame stabilization of pulsed methane jets in a hot vitiated coflow studied with high-speed laser and imaging techniques, Appl. Phys. B 108 (2012) 407–417.

[9] W. Meier, I. Boxx, C. Arndt, M. Gamba, N. Clemens, Investigation of auto-ignition of a pulsed methane jet in vitiated air using high-speed imaging techniques, J. Eng. Gas Turb. Power 133 (2010) 021504.

[10] C. M. Arndt, R. Schießl, J. D. Gounder, W. Meier, M. Aigner, Flame stabilization and auto-ignition of pulsed methane jets in a hot coflow: Influence of temperature, Proc. Combust. Inst 34 (2013) 1483–1490.

[11] M. J. Papageorge, C. M. Arndt, F. Fuest, W. Meier, J. A. Sutton, High-speed mixture fraction and temperature imaging of pulsed, turbulent fuel jets auto-igniting in high-temperature, vitiated co-flows, Exp. Fluids 55 (2014) 197–213.

[12] C. M. Arndt, M. J. Papageorge, F. Fuest, J. A. Sutton, W. Meier, M. Aigner, The role of temperature, mixture fraction, and scalar dissipation rate on transient methane injection and auto-ignition in a jet in hot coflow burner, Combust. Flame 167 (2016) 60–71.

[13] F. Eitel, J. Pareja, A. Johchi, B. Böhm, D. Geyer, A. Dreizler, Temporal evolution of auto-ignition of ethylene and methane jets propagating into a turbulent hot air co-flow vitiated with NOx, Combust. Flame 177 (2017) 193–206.

[14] A. Fiolitakis, C. M. Arndt, Transported PDF simulation of auto-ignition of a turbulent methane jet in a hot, vitiated coflow, Combust. Theory Model. 24 (2020) 326–361.

[15] E. Inanc, A. M. Kempf, Numerical study of a pulsed auto-igniting jet flame with detailed tabulated chemistry, Fuel 252 (2019) 408–416.

[16] B. Liu, J. An, F. Qin, R. Li, G. Q. He, L. Shi, D. Zhang, Large eddy simulation of auto-ignition kernel development of transient methane jet in hot co-flow, Combust. Flame 215 (2020) 342–351.

[17] E. Mastorakos, T. A. Baritaud, T. J. Poinsot, Numerical simulations of autoignition in turbulent mixing flows, Combust. Flame 109 (1997) 198–223.

[18] C. S. Yoo, R. Sankaran, J. H. Chen, Three-dimensional direct numerical simulation of a turbulent lifted hydrogen jet flame in heated coflow: flame stabilization and structure, J. Fluid Mech. 640 (2009) 453–481.

[19] H. Wu, Y. C. See, Q. Wang, M. Ihme, A Pareto-efficient combustion framework with submodel assignment for predicting complex flame configurations, Combust. Flame 162 (2015) 4208–4230.

[20] H. Wu, M. Ihme, Compliance of combustion models for turbulent reacting flow simulations, Fuel 186 (2016) 853–863.
[21] H. Wu, P. C. Ma, T. Jaravel, M. Ihme, Pareto-efficient combustion modeling for improved CO-emission prediction in LES of a piloted turbulent dimethyl ether jet flame, Proc. Combust. Inst. 37 (2019) 2267–2276.
[22] C. D. Pierce, P. Moin, Progress-variable approach for large-eddy simulation of non-premixed turbulent combustion, J. Fluid Mech. 504 (2004) 73–97.
[23] M. Ihme, C. M. Cha, H. Pitsch, Prediction of local extinction and re-ignition effects in non-premixed turbulent combustion using a flamelet/progress variable approach, Proc. Combust. Inst. 30 (2005) 793–800.
[24] E. Mastorakos, Ignition of turbulent non-premixed flames, Prog. Energy Combust. Sci. 35 (2009) 57–97.
[25] M. Ihme, L. Shunn, J. Zhang, Regularization of reaction progress variable for application to flamelet-based combustion models, J. Comput. Phys. 231 (2012) 7715–7721.
[26] D. G. Goodwin, CANTERA: An open-source, object-oriented software suite for combustion, https://cantera.org, 1998.
[27] E. Mastorakos, A. P. Pires da Cruz, T. A. Baritaud, T. J. Poinsot, A model for the effects of mixing on the autoignition of turbulent flows, Combust. Sci. Tech. 125 (1997) 243–282.
[28] Y. Khalighi, J. W. Nichols, S. Lele, F. Ham, P. Moin, Unstructured large eddy simulation for prediction of noise issued from turbulent jets in various configurations, AIAA Paper 2011-2886 (2011).
[29] P. C. Ma, Y. Lv, M. Ihme, An entropy-stable hybrid scheme for simulations of transcritical real-fluid flows, J. Comput. Phys. 340 (2017) 330–357.
[30] A. V. W. Vreman, An eddy-viscosity subgrid-scale model for turbulent shear flow: algebraic theory and applications, Phys. Fluids 16 (2004) 3670–3681.
[31] S. Gottlieb, C. W. Shu, E. Tadmor, Strong stability-preserving high-order time discretization methods, SIAM Rev. 43 (2001) 89–112.
[32] H. Wu, P. C. Ma, M. Ihme, Efficient time-stepping techniques for simulating turbulent reactive flows with stiff chemistry, Comput. Phys. Commun. 243 (2019) 81–96.
[33] M. Klein, A. Sadiki, J. Janicka, A digital filter based generation of inflow data for spatially developing direct numerical or large eddy simulations, J. Comput. Phys. 186 (2003) 652–665.
[34] S. B. Pope, Turbulent Flows, Cambridge University Press, 2000.
[35] T. Jaravel, H. Wu, M. Ihme, Error-controlled kinetics reduction based on non-linear optimization and sensitivity analysis, Combust. Flame 200 (2019) 192–206.
[36] J. M. Hall, E. L. Petersen, An optimized kinetics model for OH chemiluminescence at high temperatures and atmospheric pressures, Int. J. Chem. Kinet. 38 (2006) 714–724.
[37] O. Colin, F. Ducros, D. Veynante, T. Poinsot, A thickened flame model for large eddy simulations of turbulent premixed combustion, Phys. Fluids 12 (2000) 1843–1863.
[38] G. Nastac, J. W. Labahn, L. Magri, M. Ihme, Lyapunov exponent as a metric for assessing the dynamic content and predictability of large-eddy simulations, Phys. Rev. Fluids 2 (2017) 094606.